Chapter 13
Dielectric Materials with Hyperordered Structures

Hiroki Taniguchi

Abstract Dielectric materials with "hyperordered structures" are introduced in this section. Dielectric materials are one of the key ingredients in modern electronics, as they are used in capacitors, actuators, frequency filters, and nonvolatile memories in various devices. Recent rapid growth of information and communication technologies and power electronics has inspired vital research into the development of novel dielectric materials with high permittivity, which can boost miniaturization of electronic devices and improve the energy storage density of capacitors. A conventional way to explore high-permittivity dielectrics is to design the bulk property of materials by means of ferroelectric phase transition. Many experimental and theoretical findings, however, have suggested that imperfections of materials sometimes give rise to an extraordinarily large dielectric response, as represented by relaxors. Although individual investigations are still underway, there seems to be something beyond imperfection underlying the design of high-permittivity dielectrics, namely "hyperordered structures" (HOSs). Section 13.1 provides an overview of the fundamentals of dielectric materials. Then, Sect. 13.2 introduces several conventional concepts for designing the permittivity of homogeneous dielectric materials. Next, inhomogeneous systems that show high permittivity greater than the homogeneous systems are described in Sect. 13.3. Section 13.4 discusses one potential HOS candidate in dielectric materials, electron-pinned defect dipoles, which are the extended local structures of large polarizability that form around heterovalent ions introduced to a bulk matrix.

Keywords Dielectric · Ferroelectric · Permittivity · Defect complex · Phase transition

H. Taniguchi (✉)
Department of Physics, Nagoya University, Nagoya 464-8602, Japan
e-mail: taniguchi@nagoya-u.jp

K. Hayashi (ed.), *Hyperordered Structures in Materials*, The Materials Research Society Series, https://doi.org/10.1007/978-981-99-5235-9_13

13.1 Fundamentals of Dielectric Materials

Dielectric materials are classified as materials in which an electric polarization P appears under the application of an external electric field E. The macroscopic response of P can be described by the sum of the microscopic dipole moments μ within a unit volume V, $P = \left(\sum \mu\right)/V$. A relative electronic susceptibility χ is a coefficient between P and E, giving $P = \chi\epsilon_0 E$, where ϵ_0 is the vacuum permittivity. On the other hand, the relative dielectric permittivity ϵ is a coefficient between the electronic displacement D and E, giving $D = \epsilon\epsilon_0 E = \epsilon_0 E + P = (1+\chi)\epsilon_0 E$, thereby $\epsilon = 1 + \chi$. In contrast to the macroscopic coefficients χ and ϵ, the polarizability α defines a microscopic polar response of materials that relates μ and E as $\mu = \alpha E$. Hereafter, ϵ is called the permittivity for simplicity. The dielectric permittivity ϵ is generally a complex quantity, so it is expressed as $\epsilon = \epsilon' + i\epsilon''$. Conventionally, we use a ratio between the real and the imaginary parts of permittivity, $\tan\delta = \epsilon''/\epsilon'$, to indicate the magnitude of energy dissipation during a charge–discharge process for the dielectric materials. There are various microscopic origins for the dipole moment μ in the materials, for instance, polar molecules, the relative displacement of oppositely charged ions or particles, ferroelectric domains, accumulated carriers around the interfaces, and so on. Since each μ has an individual time scale, the dielectric response of materials shows rich frequency dispersion, as shown in Fig. 13.1. In general, the response of polar molecules, μ_{d}, gives a relaxation-type frequency dispersion, while a resonance-type frequency dispersion appears due to the response of ionic displacement, μ_{ion}, or the electronic one, μ_{e}. In contrast, the extrinsic components due to the domains, μ_{domain}, and the accumulated space charges, μ_{sc}, have a relatively slow response; therefore, their responses are usually observed in the low-frequency region below 10^6 Hz. The frequency dispersions of μ_{domain} and μ_{sc} are of the relaxation type. Note that the *extrinsic* component means that the dielectric response does not stem from an inherent nature of the material but is caused by various inhomogeneities.

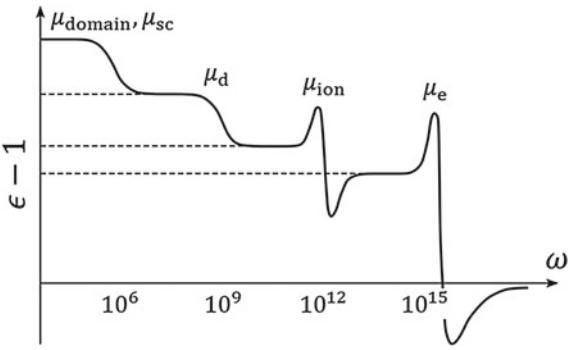

Fig. 13.1 The schematic illustration of the frequency dispersion of dielectric permittivity and the corresponding dipole components

13.2 Permittivity Engineering in a Homogeneous System

There are several ways to design dielectric materials according to a range of permittivity. For ordinary dielectric materials with permittivities 10^0–10^1, the permittivity can be roughly estimated with the additivity rule of polarizability, where the total polarizability is given by the addition of individual constituent ions, as presented in Fig. 13.2 [1]. In $Ba^{2+}B_2^{4+}O_4^{2-}$, for instance, the total polarizability of 14.54 is estimated from the ionic polarizability of Ba^{2+}, B^{4+}, and O^{2-} of 6.40, 0.05, and 2.01 in a unit of $Å^3$, respectively. The permittivity ϵ is then calculated with the Clausius–Mossotti relation, to be 6.14, where N is the number of dipole moments in a unit volume. This value is nearly equal to the experimental value of 6.05. The applicability of this concept is, however, limited to harmonic materials in which the dynamics of lattice vibrations is harmonic.

$$\frac{N\alpha}{3\epsilon_0} = \frac{\epsilon - 1}{\epsilon + 2}$$

In anharmonic materials, where some of long-wavelength lattice vibrations or the corrective fluctuations of dipole moments are unstable due to various interactions, a permittivity on the order of 10^2–10^3 is often observed. Ferroelectric materials are typical cases. Ferroelectric materials are practically defined as materials having spontaneous polarization, the direction of which can be switched by the applied electric field. From a crystallographic viewpoint, all polar materials are potentially ferroelectric. Many ferroelectric materials show a ferroelectric phase transition from a nonpolar phase to a polar phase on cooling. If a primary-order parameter of the ferroelectric phase transition is the polarization P, the permittivity ϵ divergently increases around a ferroelectric phase transition temperature. In the case of the perovskite-type oxide $BaTiO_3$, for example, the high-temperature nonpolar phase of $Pm\bar{3}m$ symmetry transforms into the low-temperature polar phase of $P4mm$ symmetry at 123 °C [2], around which the permittivity reaches the order of 10^3 (Fig. 13.3) [3]. It is known that the unstable lattice vibration, which is called the "ferroelectric soft

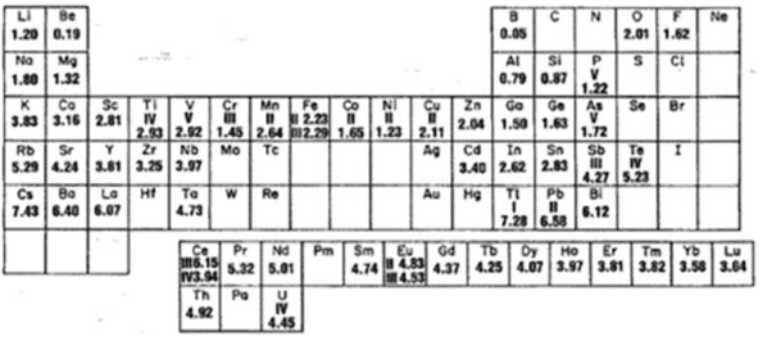

Fig. 13.2 The polarizability of ions, which is given a unit of $Å^3$ (https://doi.org/10.1063/1.353856)

mode," plays an important role in the ferroelectric phase transition of perovskite-type oxides [4]. The ferroelectric soft mode is a special transverse optical phonon mode at the Γ-point of the Brillouin zone, whose frequency decreases toward zero as the temperature approaches the ferroelectric phase transition temperature T_c due to the strong anharmonic interaction. According to the Lyddane–Sachs–Teller relation, the permittivity is inversely proportional to the square of the soft mode frequency, and the decreasing frequency of the soft mode therefore raises the permittivity of the material [5, 6]. It is known that the soft mode also enhances the permittivity of materials even in the case when the system stays paraelectric until zero Kelvin. A typical example can be seen in the rutile-type TiO_2, whose permittivity reaches 270 along the crystallographic [001] direction in the low-temperature region (Fig. 13.4) [7]. The soft mode in the rutile-type TiO_2 decreases its frequency to raise the permittivity as the temperature decreases but never reaches zero at finite temperatures [8]. This behavior is called "incipient ferroelectricity." Quantum paraelectricity in $SrTiO_3$ is a special case of incipient ferroelectricity, where the system tends to go ferroelectric at a finite temperature but is suppressed by quantum fluctuation [9]. A delicate balance between the soft mode instability and the quantum fluctuation gives rise to the extremely large permittivity of the order of 10^3–10^4 in the low-temperature region [10].

Several concepts for designing ferroelectric materials have recently been established in perovskite type and related oxides owing to the development of theoretical and experimental techniques. Covalency between oxygen and constituent ions is one of the clues for internal distortion within coordination polyhedra [11, 12], and a comparison between $CaTiO_3$ and $CdTiO_3$ provides a good example [13–15]. These compounds crystallize in the same orthorhombic crystal structure of centrosymmetric *Pnma*(*Pbnm*) symmetry at room temperature, where oxygen octahedra rotate as $a^+b^-b^-$ in Glazer's notation [16, 17]. $CdTiO_3$ undergoes a ferroelectric phase transition to the polar $Pna2_1$ structure at $T_c \sim 85$ K [18], whereas $CaTiO_3$ remains in the *Pnma* structure until 0 K. Figure 13.5 presents the temperature dependence of dielectric permittivity in $(Cd_{1-x}Ca_x)TiO_3$ with the Ca concentration $x = 0$–0.05. In

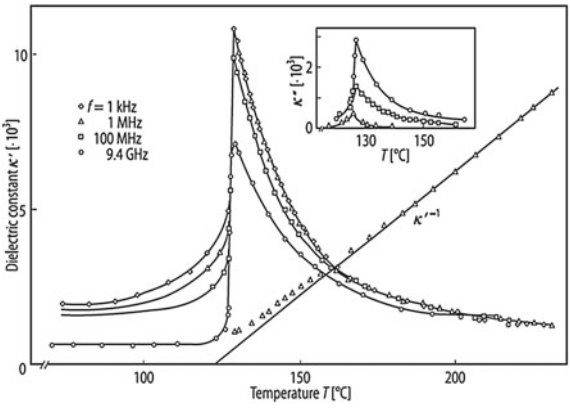

Fig. 13.3 Temperature dependence of the dielectric permittivity of $BaTiO_3$ ceramics measured with various frequencies. See details in Ref. [3] (https://doi.org/10.1080/00150198808008805)

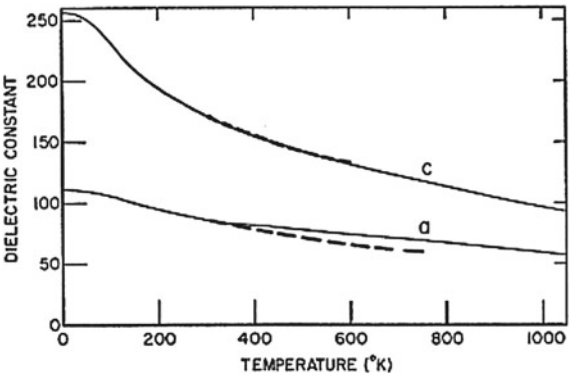

Fig. 13.4 Temperature dependence of the dielectric permittivity of a rutile-type TiO_2 single crystal, which is measured along the tetragonal a and c axes (https://doi.org/10.1103/PhysRev.124.1719)

the composition for $x = 0$, as shown in the figure, the permittivity rapidly increases as the temperature approaches T_c. The ferroelectric transition temperature T_c decreases with increments of x, indicating suppression of ferroelectric instability due to the Ca substitution. The Ca-concentration dependence of T_c, presented in the inset of Fig. 13.5, indicates that the ferroelectricity disappears around $x = 0.05$. In simple terms, the covalency can be measured by the difference in electronegativity; the closer the electronegativity, the stronger the covalency. In the case of $(Cd_{1-x}Ca_x)TiO_3$, Cd has stronger covalency with O than Ca, because the electronegativity of Cd and Ca are 1.69 and 1.00, respectively, whereas that of O is 3.44. Figure 13.6 shows the electronic density of states (DOS) for $CdTiO_3$ and $CaTiO_3$, which are obtained with first-principles calculations, where partial DOSs for the s-orbital of Cd(Ca) and p-orbital of O are denoted by red and blue hatches. Compared to the $CaTiO_3$, $CdTiO_3$ has larger overlap between the s- and p-orbitals, visualizing a stronger covalency of Cd–O than Ca–O. From a crystallographic viewpoint, the *Pnma* structure of $CdTiO_3$ has one symmetric O–Cd–O bond along the [010] direction, in addition to two asymmetric O–Cd–O bonds along the [101] and [−101] directions (Fig. 13.7). Although the asymmetric O–Cd–O bonds generate local dipole moments, they mutually cancel out to net zero polarization within the plane normal to [010]. Along the [010] direction, in contrast, the symmetric O–Cd–O bond induces no dipole moment intrinsically in the paraelectric phase. Like the O–Cd–O bonds along the [101] and [−101] directions, the Cd atom in O–Cd–O along the [010] direction also possesses the tendency to displace toward one of the adjacent oxygen atoms due to the strong covalency of Cd–O. In a sufficiently high-temperature region, however, thermal fluctuation leads to an average position of Cd at the center of the O–Cd–O bond, thus rendering the macroscopic symmetry centrosymmetric. As the thermal fluctuation decreases on cooling, the effect of covalency becomes more dominant, and the Cd displaces to induce the dipole moment below the specific temperature T_c. This picture can also be seen from the viewpoint of the lattice vibration. Figure 13.8a presents the phonon dispersion curves of $CdTiO_3$, which are calculated in the paraelectric phase of the *Pnma* structure, where a position on the vertical axis below zero indicates an imaginary frequency. At the Γ-point ($k = 0$) in the figure, the frequency of one optical

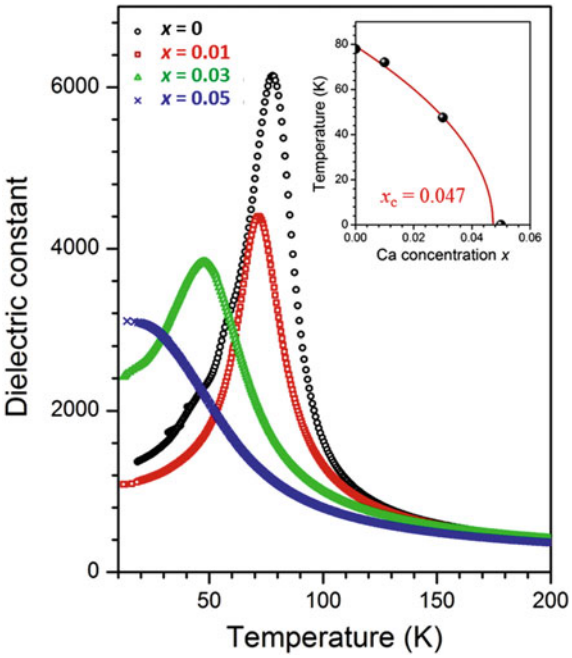

Fig. 13.5 Temperature dependence of the dielectric permittivity in $(Cd_{1-x}Ca_x)TiO_3$ with the Ca concentration $x = 0$–0.05. The inset presents a variation of the ferroelectric phase transition temperature T_c as a function of the Ca content x

phonon branch is found to be imaginary, indicating that its vibration is unstable in the *Pnma* structure without any support from thermal fluctuation. This mode is the ferroelectric soft mode of $CdTiO_3$, which drives the phase transition. A displacement pattern of the ferroelectric soft mode is shown in Fig. 13.8b. As shown in the figure, Cd atoms oscillate between two adjacent oxygens, and freezing this vibration at the ferroelectric phase transition temperature T_c induces the polar displacement of Cd in the O–Cd–O bond. Note that the reason why the ferroelectric displacement of Cd atoms at $k = 0$ is more energetically favorable than the non-ferroelectric displacement at $k \neq 0$ is beyond the present scope. It is probable that a further concept is required to deduce the energetics of an O–Cd–O–Cd–O extended bond in an intuitive way.

13.3 Permittivity Engineering in an Inhomogeneous System

Designing dielectric materials with a permittivity greater than 10^4 often requires the extra contribution from the inhomogeneity in materials in order to increase the dielectric response. Typical examples are polar nano regions (PNRs) in relaxors [19–24]. Relaxors are categorized as materials that show a broad and dispersive peak in the temperature dependence of dielectric permittivity. The temperature at which the permittivity reaches the cusp, T_m, strongly depends on a frequency of AC voltage used

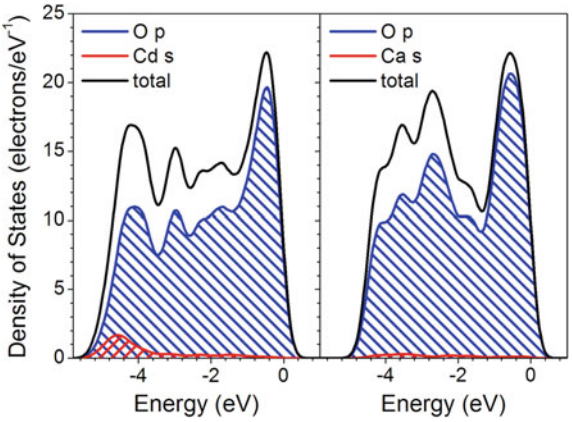

Fig. 13.6 Electronic density of states (DOS) for $CdTiO_3$ and $CaTiO_3$, where partial DOSs for the s-orbital of Cd(Ca) and p-orbital of O are denoted by positive and negative slope lines

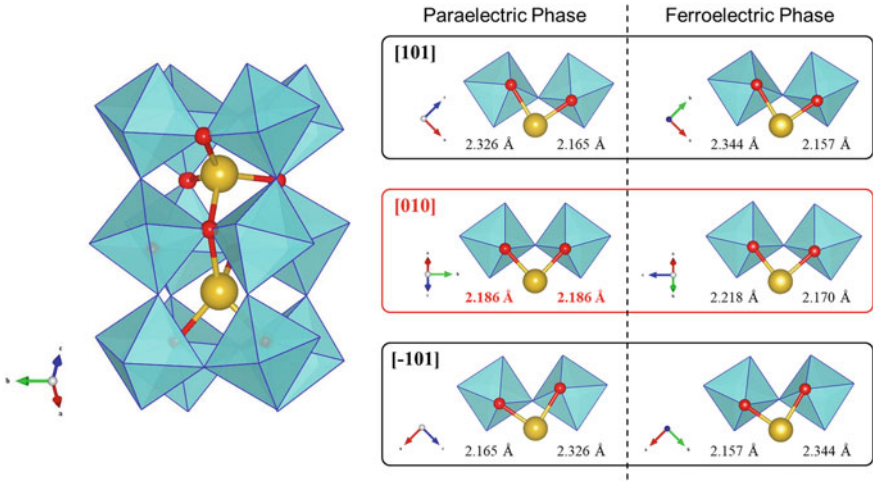

Fig. 13.7 Schematic illustrations for the O–Cd–O bonds in $CdTiO_3$ at the paraelectric and ferroelectric phases. The large yellow spheres, small red spheres, and octahedra in the figure denote the Cd atoms, O atoms, and TiO_6 units, respectively

in the dielectric measurement, where T_m shifts to the higher temperature region as the frequency elevates (Fig. 13.9). When we estimate a relaxation time τ_m from a specific frequency f_m ($= 1/\tau_m$), at which the imaginary part of the permittivity culminates, as a function of temperature, the relation between τ_m and the temperature follows the Vogel–Fulcher law, $\tau_m = \tau_0 \exp(E_a/k_B(T_m - T_f))$, indicating growing clusters in the system [25, 26]. Many studies have clarified the polar clusters of several tens of nanometers, which are called PNRs, as they grow on cooling, imparting an extrinsic

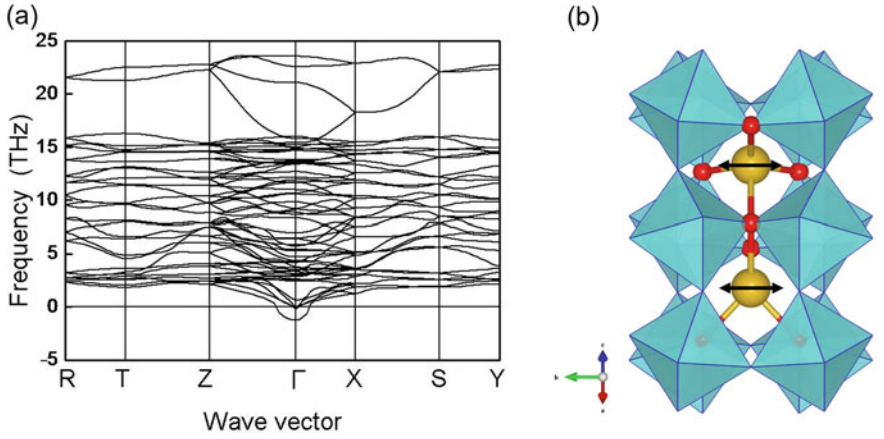

Fig. 13.8 **a** The phonon dispersion for the paraelectric phase of $CdTiO_3$, which is obtained by first-principles calculation at 0 K. **b** A displacement pattern of the ferroelectric soft mode in $CdTiO_3$, where the large yellow spheres, small red spheres, and octahedra denote Cd atoms, O atoms, and TiO_6 units, respectively. The arrows in the figure schematically indicate the amplitude of the Cd oscillation in the soft mode

polarization response to the applied electric field to improve dielectric permittivity over a wide temperature range around T_m [19–27]. The PNRs often arise because of a disturbance in the long-range polar ordering due to the ferroelectric phase transition resulting from atomic-scale heterogeneity in the system.

$Pb(Mg_{1/3}Nb_{2/3})O_3$ (PMN) is a typical relaxor material with a perovskite-type crystal structure that has been widely studied to date. In PMN, Mg–Nb one-to-one complexes with negative charge, which are called chemically ordered regions (CORs), serve as a source of a quenched random electric field in the matrix [28–30]. PMN has intrinsic ferroelectric instability, as a previous Raman scattering study demonstrates. Figure 13.10 shows the temperature dependence of Raman spectra that were observed in the PMN single crystal [31]. As shown in the figure, the low-frequency component gradually grows as the temperature approaches $T_c \sim 200$ K. Note that, according to Fu et al. [24], T_c in PMN in this context is defined as the temperature at which the permittivity takes a maximum under the application of an electric field sufficiently high to induce long-range polar ordering, although the relaxors do not have a definite transition temperature under a zero electric field. The temperature dependence of the frequency for the low-frequency component, which is estimated by spectral analyses, is plotted in Fig. 13.11, along with a typical temperature dependence of the soft mode observed in $CdTiO_3$. In the figure, the blue, red, and black circles denote the harmonic frequency for the soft mode ω_{s0}, damping constant for the soft mode's vibration γ_s, and the soft mode frequency ω_s $(= \sqrt{\omega_{s0}^2 - \gamma_s^2})$, respectively. The figure shows that, in both cases for PMN and $CdTiO_3$, the soft mode frequency ω_s decreases as the temperature approaches T_c, indicating the typical soft mode-driven phase transition. In contrast to the qualitative

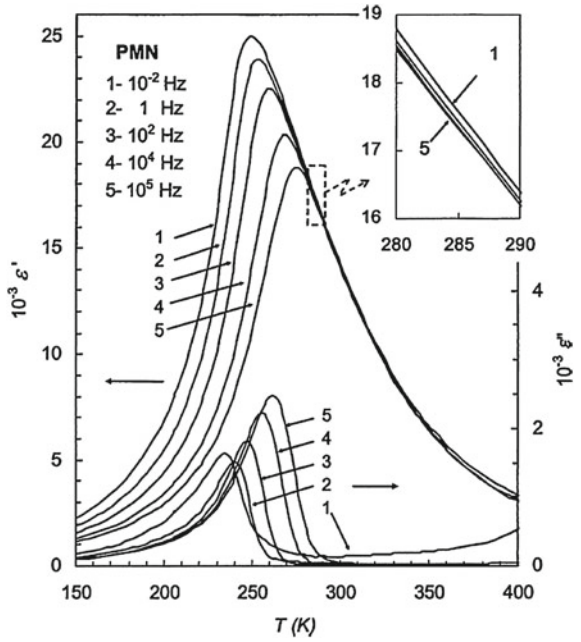

Fig. 13.9 Temperature dependence of real and imaginary parts of dielectric permittivity in $Pb(Mg_{1/3}Nb_{2/3})O_3$ (PMN), which is measured at various frequencies (https://doi.org/10.1007/s10853-005-5915-7)

similarity in the softening behavior, the temperature scale is markedly extended in PMN compared to $CdTiO_3$. The difference in the soft mode dynamics is also seen in the stability of the oscillation, which can be evaluated by a relation between ω_s and γ_s; the oscillation of the soft mode is stable in an *underdamped* region of $\omega_{s0} > \gamma_s$, whereas it is unstable in an *overdamped* region of $\omega_{s0} < \gamma_s$. As shown in Fig. 13.11, a wide *overdamped* region spreads before the transition temperature, suggesting that the spatial inhomogeneity fractionates a coherent length of the soft mode to disturb the long-range polar ordering. Such a localized soft mode is a potential mechanism for the formation of PNR and the relaxor phenomena [24, 31, 32].

A barrier layer capacitor (BLC) effect is the other concept leading to permittivity greater than 10^4, although it is not the true permittivity but an apparent one. In the perovskite-related paraelectric $CaCu_3Ti_4O_{12}$ (CCTO), a permittivity on the order of 10^4 is observed over a wide frequency range below 10^6 Hz (Fig. 13.12) [33, 34]. In marked contrast to the case of ferroelectric materials that show a high permittivity only around T_c, the permittivity here shows little temperature dependence over a wide temperature region, depending on the frequency (Fig. 13.13) [35]; in the case of the frequency of 1.37 kHz, for instance, the high permittivity survives until approximately 100 K, as presented in Fig. 13.13. Upon further cooling, the permittivity steeply decreases to the order of 10^1. This kind of dielectric response is known to stem from electric inhomogeneity in the material due to, for instance, a core–shell structure of grains and/or several kinds of dislocations, where one part of the material is semiconducting and the other is insulating [36–38]. Figure 13.14 shows (a) the topography and (b) the current image of the CCTO ceramics sample,

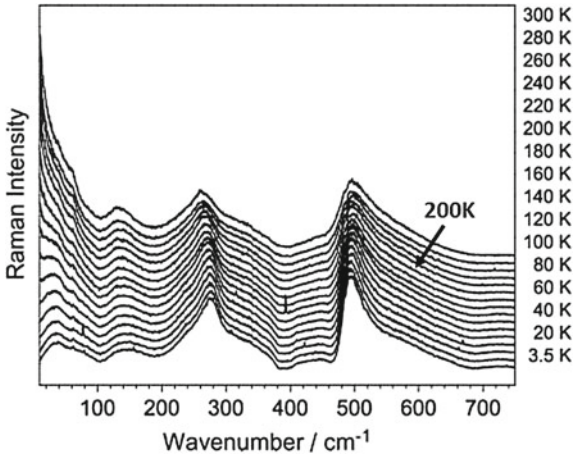

Fig. 13.10 Temperature dependence of Raman spectra observed in the PMN single crystal (https://doi.org/10.1002/jrs.2746)

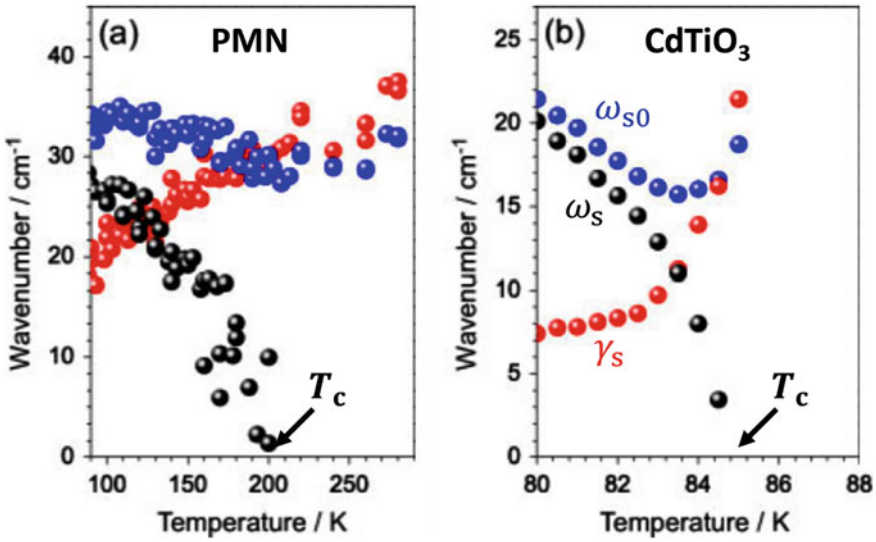

Fig. 13.11 **a** Temperature dependence of the harmonic frequency for the soft mode ω_{s0} (blue), damping constant γ_s (red), and the soft mode frequency ω_s ($= \sqrt{\omega_{s0}^2 - \gamma_s^2}$) (black) for **a** PMN and **b** $CdTiO_3$, where the mode frequency is plotted in terms of cm^{-1} according to convention (https://doi.org/10.1002/jrs.2746)

as observed by atomic force microscopy (AFM). The contrast in panel (b) indicates the magnitude of the observed current under application of bias voltage, where the darker color denotes the larger current. As shown in magnified images for the grain and the grain boundary, which are respectively presented in panels (c) and (d), there is an inhomogeneous distribution of electric conductivity in the sample. The spatial scale of the inhomogeneity is found to be on the order of a nanometer, as indicated in the panel. The line profile of the observed electric current along the line from E to F in the panel (b) is shown in the panel (e). Panel (f) presents the results of local I–V measurements performed in selected areas in the inside of the grain and around the grain boundary, as labeled in panel (b). As shown in the figure, an insulating property is found in areas A and B, whereas relatively large electric conduction is detected in areas C and D. When an electric field is applied to a system with such an electric inhomogeneity, the carriers are blocked by the insulating area after traveling within the conductive area to induce huge dielectric displacement. This behavior can be modeled by the system with two different components aligned in series, as presented in Fig. 13.15, where they have mutually different electric properties mimicking the conducting and the insulating areas in the material. Figure 13.15 also presents the temperature dependence of the dielectric permittivity and the loss of two CCTO samples with the solid curves, where #A and #B are the as-synthesized and the post-annealed samples, respectively (See Ref. [37] for details). The simulated curves with the equivalent circuit model are plotted with broken lines in the figure, where the activation energies used in the simulations are experimentally determined with an Arrhenius plot in the inset. As presented in the figure, the simulated curves are in good agreement with experiment and confirm that the huge permittivity in CCTO stems from the BLC effect, which is discussed in the Sect. 13.3. This kind of dielectric phenomenon is also called the Maxwell–Wagner effect [39].

13.4 Toward Functional Local Structures in Dielectric Materials

As introduced in the preceding section, local structures often play a role in enhancing the permittivity. Considering the additivity rule of polarizability, the creation of a unique local structure with extremely large polarizability in a homogeneous medium will probably raise the permittivity markedly. This idea provides a way for designing "hyperordered structures (HOSs)" in dielectric materials. Electron-pinned defect-dipoles (EPDDs), which were reported in 2013, would be categorized as a local structure of this type [40].

It has been reported that, when Ti of the rutile-type TiO_2 is slightly substituted by the same amount of Nb and In, the permittivity of TiO_2 markedly increases to the order of 10^4 over a wide frequency range from 10^1 to 10^6 Hz (Fig. 13.16). As shown in the figure, only 0.05% of co-dopants are found to lift the permittivity to approximately 2×10^4 with tanδ smaller than 10^{-1}. As the concentration of co-dopants increases

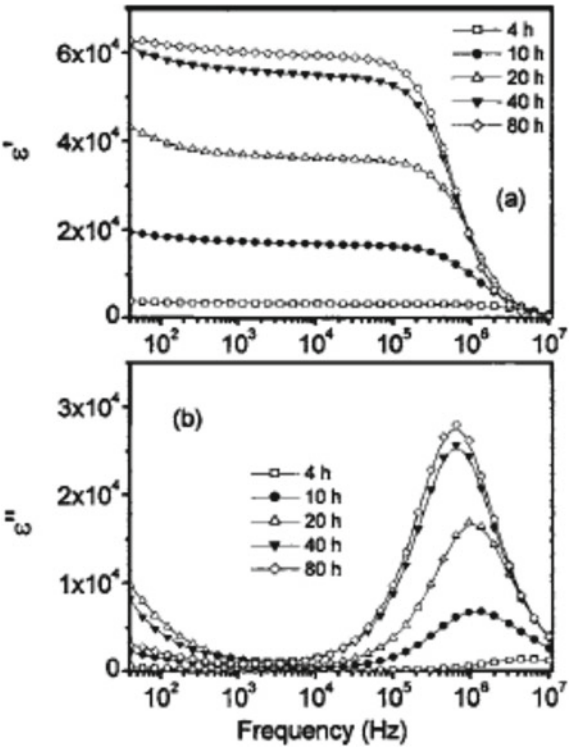

Fig. 13.12 (Top) Real and (bottom) imaginary parts of the dielectric permittivity of CCTO at room temperature as a function of frequency. The data are measured in the samples with different sintering times (https://doi.org/10.1063/1.2077864)

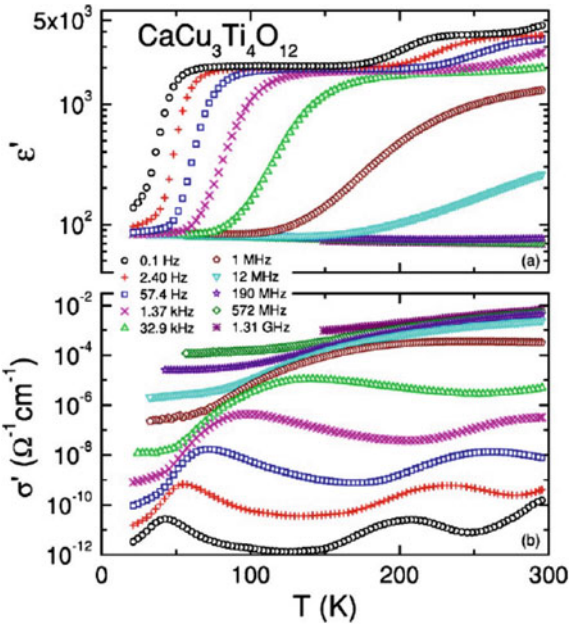

Fig. 13.13 Temperature dependence of (top) permittivity and (bottom) resistivity of CCTO measured with various frequencies (https://doi.org/10.1103/PhysRevB.70.172102)

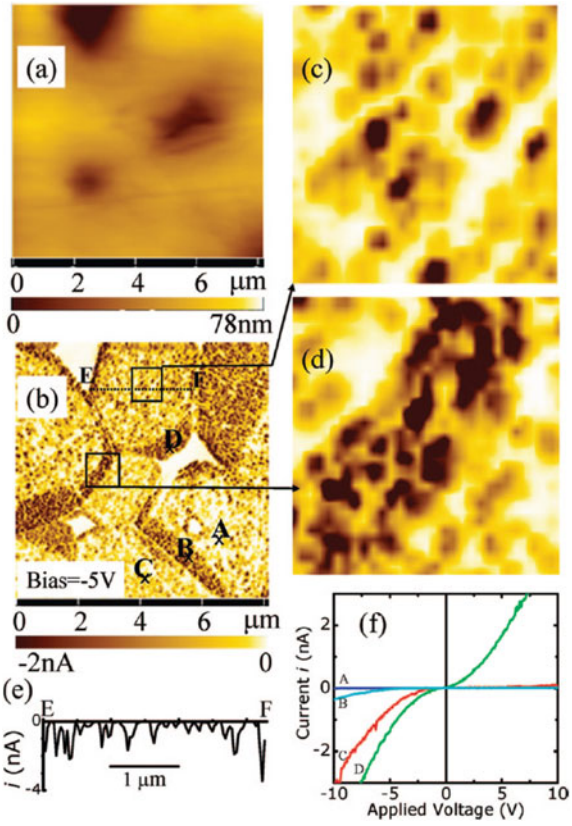

Fig. 13.14 **a** The surface topology and **b–d** the current image of CCTO ceramics observed with atomic force microscopy (AFM). **e** The line profile of current measured between the points E and F in panel **b**. The *I–V* properties measured at the points A, B, C, and D in panel **b** (https://doi.org/10.1021/cm0710507)

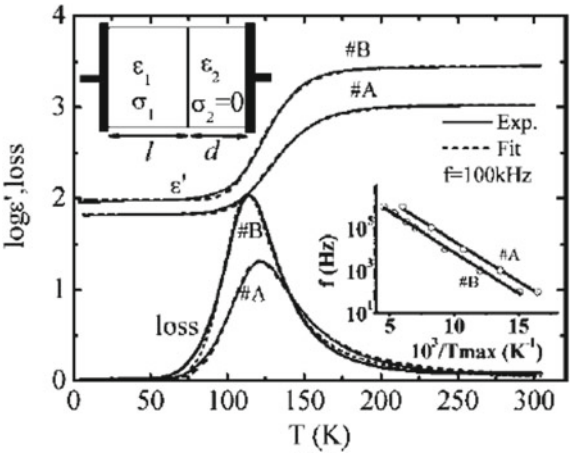

Fig. 13.15 The two-components model describing the dielectric properties of CCTO. See text for details (https://doi.org/10.1021/cm0710507)

to 10%, furthermore, the permittivity reaches 6×10^4, keeping the value of tanδ sufficiently small. An origin of this remarkable effect was initially attributed to the special complex defect pair, called EPDD. Figure 13.17 presents the schematic illustration of EPDD, which is deduced by first-principles calculations. As shown in the figure, the co-substitution of Nb and In introduces two types of defect complexes, $In_2^{3+}V_O^{\cdot\cdot}Ti^{3+}$ and $Nb_2^{5+}Ti^{3+}A_{Ti}$ ($A_{Ti} = Ti^{3+}$, Ti^{4+}, or In^{3+}), and their overlap forms the highly polarizable extended defect complex, EPDD. Such an extended local structure can be regarded as HOS, which enables marked enhancement of the permittivity in dielectric materials. Several follow-up studies, however, pointed out that the BLC effect contributes to the observed high permittivity [40–45]. Presented in Fig. 13.18 is a current–voltage plot for 1% Nb + In co-doped TiO_2 (NITO-1%) ceramics, which is measured in several characteristic areas of the sample. Panel (a) shows an optical microscopic image of the NITO-1% ceramic sample on which micro-electrodes are attached (bright areas). The current–voltage property was measured between the electrodes of 1–2, 1–3, and 3–4. There is no grain boundary between the electrodes 1–2, whereas 1–3 and 3–4 run across the grain boundaries. Between the electrodes 1–2, as plotted in panel (b), large current flows show a semiconductive property of the grain core. Between the electrodes 1–3 and 3–4, in contrast, the current is found to be very small under the application of an electric field, indicating a highly insulating property of the grain boundaries. This result clarifies the BLC effect due to the core–shell structure of grains in NITO-1%. It should be noted that Nb^{5+} and In^{3+} are nominally chosen to avoid generation of Ti^{3+}, which seriously deteriorates the insulating property of TiO_2. The observed semiconducting property is probably due to the spatial inhomogeneity of the Nb-to-In ratio, which induces partial generation of Ti^{3+} in the sample.

Despite the negative experimental results for the EPDD concept, dielectric measurements in the low-temperature region, in which the semiconducting property of co-doped TiO_2 is suppressed, suggests that the concept of EPDD itself works, although the enhancement of permittivity is not as large as initially reported. Figure 13.19 presents the (a) real and (b) imaginary parts of the dielectric permittivity of NITO-0.5% single crystal along the crystallographic *c*-direction, which are measured as a function of temperature and frequency. At 30 K, NITO-0.5% shows a permittivity on the order of 10^4 over the frequency range from 10^3 to 10^6 Hz, indicating that the sample remains semiconducting in this temperature region. As the temperature decreases, the real part of the permittivity steeply falls, as in the case of CCTO. The decrease in permittivity occurs from the higher frequency and accompanies a peak-like anomaly in the imaginary part of the permittivity, indicating a typical dielectric relaxation for the BLC effect. Figure 13.19c shows the Arrhenius plot for the observed dielectric relaxation, in which the peak frequency of the imaginary part of the permittivity is plotted as a function of temperature inverse on a single logarithmic scale. The experimental results are found to follow the Arrhenius low with an activation energy of 7.6 meV for the carrier excitation. At the lowest temperature region of approximately 2 K, where the thermally excited carriers are sufficiently suppressed to recover the fine insulation of the sample, the real part of

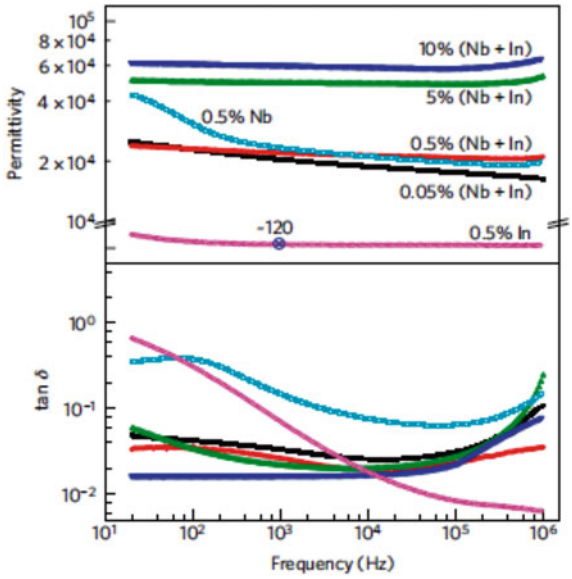

Fig. 13.16 (Top) Dielectric permittivity and (bottom) tanδ of Nb + In co-doped TiO_2 with several co-dopant concentrations, which are potted as a function of frequency (https://doi.org/10.1038/nmat3691)

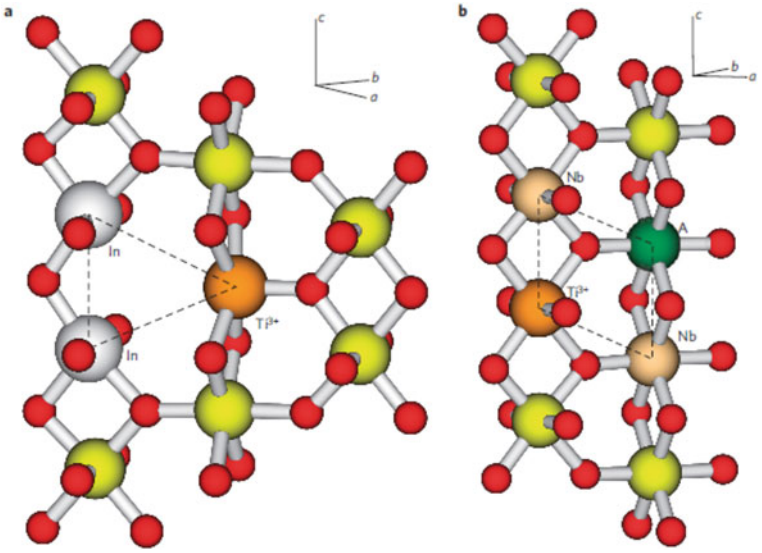

Fig. 13.17 The structure of the electron-pinned defect-dipole (EPDD), which is obtained by first-principles calculations. (https://doi.org/10.1038/nmat3691)

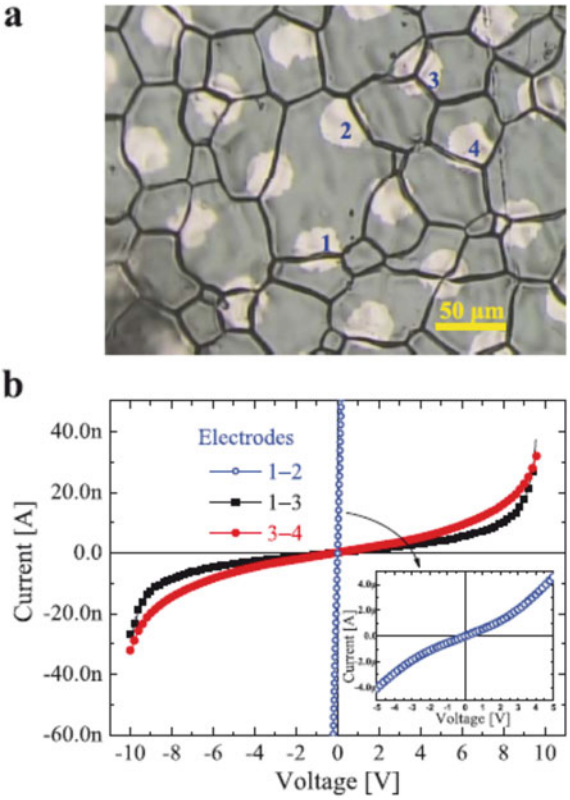

Fig. 13.18 **a** The scanning electron microscopy image of Nb + In co-doped TiO_2 ceramics, where the bright spots are electrodes. **b** *I*–*V* properties measured with the electrodes of 1–2, 1–3, and 3–4 (https://doi.org/10.1038/srep08295)

the permittivity decreases to the order of 10^2. The dielectric permittivity of NITO-0.5%, which is measured along the [001] and [110] directions at 2 K, is presented in Fig. 13.20 with the results of the pristine TiO_2. As presented in the figure, NITO-0.5% shows a permittivity of approximately 900 over a wide frequency range, from 10^2 to 10^6 along [001]. This value is more than three times greater than that for the pristine TiO_2, indicating the intrinsic permittivity enhancement due to the co-doping of Nb and In, although its magnitude is not as large as the order of 10^4 that was originally reported in Ref. [40]. Along the direction of [110], on the other hand, the permittivity of NITO-0.5% reaches 250, whereas it is 130 for the pristine TiO_2. The enhancement of permittivity is found to be more remarkable along the [001] direction than along [110]. This anisotropy suggests the anisotropic polarization property of the co-doping-induced EPDD in TiO_2.

Although the expected configuration of EPDD was reported based on first-principles calculations, its real structure has remained an open question. The EPDDs form through the weak doping of heterovalent ions in the host matrix. Their structure

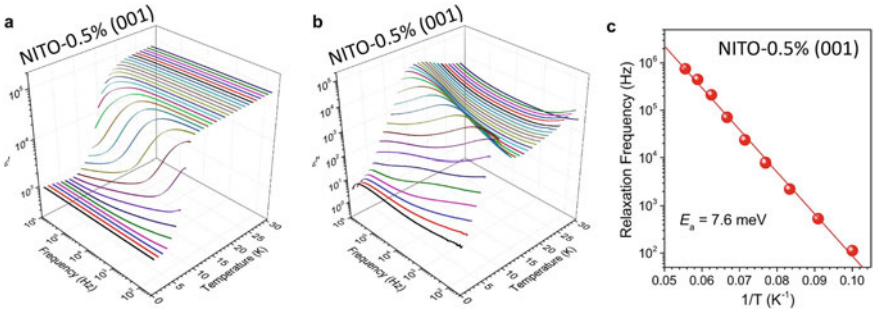

Fig. 13.19 **a** The real and **b** imaginary parts of dielectric permittivity of Nb + In co-doped TiO_2, which are potted as a function of temperature and frequency. **c** The Arrhenius plot for the dielectric relaxation, which is observed in the low-temperature region

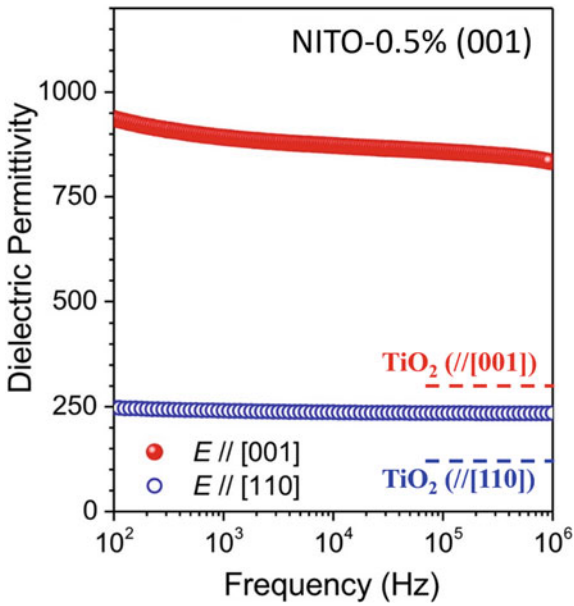

Fig. 13.20 The frequency dispersion of the dielectric permittivity of Nb + In co-doped TiO_2, which is measured along the [001] and [110] directions at 2 K. The broken lines in the figure denote the dielectric permittivity of the pristine TiO_2 at 4 K

is expected to depend strongly not only on the choice of the dopants and the crystal structure and physical properties of the host materials, but also on the synthesis conditions and concentration ratio of dopants. In Nb + In co-doped TiO_2, for instance, the amounts of Nb^{5+} and In^{3+} are nominally chosen to be the same to realize the average valence of 4+ that is the same as Ti^{4+} in TiO_2. If this condition is perfectly satisfied in the system, the co-doped sample is expected to remain insulating and no BLC effect will appear. The observed huge permittivity thus indicates a partial nonstoichiometry and/or segregation of the dopants. In this situation, the structure of EPDD would be different from that calculated under the assumption of homogeneity and perfect

stoichiometry. Nevertheless, EPDD is undoubtedly one of the fascinating concepts contributing to the development of novel dielectric materials with high permittivity in terms of HOS engineering.

13.5 Summary

This section provides an overview of permittivity engineering in dielectric materials. There are several concepts according to the range of permittivity: the additivity rule of polarizability for permittivities of 10^0–10^1, the ferroelectric phase transition for permittivities of 10^2–10^3, and the special inhomogeneities for permittivities greater than 10^4, including the relaxors and the coexistence of multiple components with different electric properties that cause the BLC effect. The new concept of local structure engineering for permittivity boosting, EPDD, was also introduced in reference to recent studies. If we envisage the HOSs as extended local structures to enhance the permittivity, which are induced by synergy between the local and the bulk properties, the PNR in the relaxors can come under this category. Active explorations and investigations of EPDD with state-of-art experimental techniques and large-scale calculations are now expanding the frontier of functional HOSs in dielectric materials. Although not discussed in this section, modified structures around twin and anti-phase boundaries would provide a rich prospect for HOSs with exotic properties. Not only in ground states, field-induced local structures such as photo-excited defect states are also potential targets for the development of HOSs of excellent functionalities that are useful for practical applications.

Acknowledgements This work was supported by JSPS KAKENHI grant numbers JP20H05878 and JP20H05879.

References

1. Shannon RD (1993) J Appl Phys 73:348
2. Sakayori K, Matsui Y, Abe H, Nakamura E, Kenmoku M, Hara T, Ishikawa D, Kokubu A, Hirota K, Ikeda T (1995) Jpn J Appl Phys 34:544
3. Kersten O, Rost A, Schmidt G (1988) Ferroelectrics 81:31
4. Scott JF (1974) Rev Mod Phys 46:83
5. Lyddane RH, Sachs RG, Teller E (1941) Phys Rev 59:673
6. Barker AS Jr (1975) Phys Rev B 12:4071
7. Parker RA (1961) Phys Rev 124:1719
8. Traylor JG, Smith HG, Nicklow RM, Wilkinson MK (1971) Phys Rev B 3:3457
9. Müller KA, Burkard H (1979) Phys Rev B 19:3593
10. Taniguchi H, Itoh M, Yagi T (2007) Phys Rev Lett 99:017602
11. Cohen RE (1992) Nature 358:136–138
12. Kuroiwa Y, Aoyagi S, Sawada A, Harada J, Nishibori E, Takata M, Sakata M (2001) Phys Rev Lett 87:217601

13. Taniguchi H, Soon HP, Shimizu T, Moriwake H, Shan YJ, Itoh M (2011) Phys Rev B 84:174106
14. Moriwake H, Kuwabara A, Fisher CAJ, Taniguchi H, Itoh M, Tanaka I (2011) Phys Rev B 84:104114
15. Taniguchi H, Soon HP, Moriwake H, Shan YJ, Itoh M (2012) Ferroelectrics 426:268–273
16. Sasaki S, Prewitt CT, Bass JD, Schulze WA (1987) Acta Cryst C43:1668–1674
17. Glazer AM (1972) Acta Cryst B28:3384–3392
18. Shan YJ, Mori H, Tezuka K, Imoto H, Itoh M (2003) Ferroelectrics 284:107–112
19. Burns G, Dacol FH (1983) Phys Rev B 28:2527–2530
20. Cross LE (1987) Ferroelectrics 76:241–267
21. Bokov AA, Ye Z-G (2006) J Mater Sci 41:31–52
22. Cowley RA, Gvasaliya SN, Lushnikov SG, Roessli B, Rotaru GM (2011) Adv Phys 60:229–327
23. Hirota K, Ye Z-G, Wakimoto S, Gehring PM, Shirane G (2002) Phys Rev B 65:104105
24. Fu D, Taniguchi H, Itoh M, Koshihara S, Yamamoto N, Mori S (2009) Phys Rev Lett 103:207601
25. Pirc R, Blinc R (2007) Phys Rev B 76:020101(R)
26. Viehland D, Jang S, Cross LE, Wuttig M (1991) Philos Mag B 64:335–344
27. Samara GA (2003) J Phys Condens Matter 15:R367–R411
28. Hilton AD, Barber DJ, Randall CA, Shrout TR (1990) J Mater Sci 25:3461
29. Boulesteix C, Varnier F, Llebaria A, Husson E (1994) J Solid State Chem 108:141
30. Chen J, Chan HM, Harmer MP (1989) J Am Ceram Soc 72:593
31. Taniguchi H, Itoh M, Fu D (2011) J Raman Spectrosc 42:706–714
32. Manley ME, Lynn JW, Abernathy DL, Specht ED, Delaire O, Bishop AR, Sahul R, Budai JD (2014) Nat Commun 5:3683
33. Adams TB, Sinclair DC, West AR (2002) Adv Mater 14:1321–1323
34. Zhang JL, Zheng P, Wang CL, Zhao ML, Li JC, Wang JF (2005) Appl Phys Lett 87:142901
35. Lunkenheimer P, Fichtl R, Ebbinghaus SG, Loidl A (2004) Phys Rev B 70:172102
36. Sinclair DC, Adams TB, Morrison FD, West AR (2002) Appl Phys Lett 80:2153
37. Fu D, Taniguchi H, Taniyama T, Itoh M, Koshihara S (2008) Chem Mater 20:1694–1698
38. Yu J, Ishikawa T, Arai Y, Yoda S, Itoh M, Saita Y (2005) Appl Phys Lett 87:252904
39. von Hippel A (1954) Dielectrics and waves. Willey, New York
40. Hu W, Liu Y, Withers RL, Frankcombe TJ, Norén L, Snashall A, Kitchin M, Smith P, Gong B, Chen H, Schiemer J, Brink F, Wong-Leung J (2013) Nat Mater 12:821–826
41. Li J, Li F, Li C, Yang G, Xu Z, Zhang S (2015) Sci Rep 5:8295
42. Song Y, Wang X, Sui Y, Liu Z, Zhang Y, Zhan H, Song B, Liu Z, Lv Z, Tao L, Tang J (2016) Sci Rep 6:21478
43. Kawarasaki M, Tanabe K, Terasaki I, Fujii Y, Taniguchi H (2017) Sci Rep 7:5351
44. Taniguchi1 H, Ando K, Terasaki I (2017) Jpn J Appl Phys 56:10PC02
45. Taniguchi H, Sato D, Nakano A, Terasaki I (2020) J Mater Chem C 8:13627–13631